Computers in Biology and Medicine 138 (2021) 104881

Contents lists available at ScienceDirect

Computers in Biology and Medicine

journal homepage: www.elsevier.com/locate/compbiomed

A numerical study to investigate the effects of tumour position on the treatment of bladder cancer in mice using gold nanorods assisted photothermal ablation

Jason KK. Cheong [a,e], Viktor Popov [a], Elisa Alchera [b], Irene Locatelli [b], Massimo Alfano [b], Luca Menichetti [c], Paolo Armanetti [c], Mirko Maturi [d], Mauro Comes Franchini [d], Ean H. Ooi [a,e,*], Yeong S. Chiew [e]

[a] Ascend Technologies Ltd, Southampton Science Park, 2 Venture Road, SO16 7NP, Southampton, United Kingdom
[b] Division of Experimental Oncology/Unit of Urology, URI, IRCCS, Ospedale San Raffaele, Milan, Italy
[c] Istituto di Fisiologia Clinica, Sede Principale, Via G. Moruzzi 1, 56124, Pisa, Italy
[d] Department of Industrial Chemistry Toso Montanari, University of Bologna, Viale Risorgimento 4, 40136, Bologna, Italy
[e] School of Engineering and Advanced Engineering Platform, Monash University Malaysia, Jalan Lagoon Selatan, 47500, Bandar Sunway, Selangor, Malaysia

ARTICLE INFO

Keywords:
Bladder cancer
Laser therapy
Nanoparticles
GNR
Thermal therapy

ABSTRACT

Gold nanorods assisted photothermal therapy (GNR-PTT) is a new cancer treatment technique that has shown promising potential for bladder cancer treatment. The position of the bladder cancer at different locations along the bladder wall lining can potentially affect the treatment efficacy since laser is irradiated externally from the skin surface. The present study investigates the efficacy of GNR-PTT in the treatment of bladder cancer in mice for tumours growing at three different locations on the bladder, i.e., Case 1: closest to skin surface, Case 2: at the bottom half of the bladder, and Case 3: at the side of the bladder. Investigations were carried out numerically using an experimentally validated framework for optical-thermal simulations. An *in-silico* approach was adopted due to the flexibility in placing the tumour at a desired location along the bladder lining. Results indicate that for the treatment parameters considered (laser power 0.3 W, GNR volume fraction 0.01% v/v), only Case 1 can be used for an effective GNR-PTT. No damage to the tumour was observed in Cases 2 and 3. Analysis of the thermo-physiological responses showed that the effectiveness of GNR-PTT in treating bladder cancer depends not only on the depth of the tumour from the skin surface, but also on the type of tissue that the laser must pass through before reaching the tumour. In addition, the results are reliant on GNRs with a diameter of 10 nm and an aspect ratio of 3.8 - tuned to exhibit peak absorption for the chosen laser wavelength. Results from the present study can be used to highlight the potential for using GNR-PTT for treatment of human bladder cancer. It appears that Cases 2 and 3 suggest that GNR-PTT, where the laser passes through the skin to reach the bladder, may be unfeasible in humans. While this study shows the feasibility of using GNRs for photothermal ablation of bladder cancer, it also identifies the current limitations needed to be overcome for an effective clinical application in the bladder cancer patients.

1. Introduction

Bladder cancer is deadly and if left untreated, can result in death in 85% of the patients within 2 years of diagnosis [1]. Current methods for treating bladder cancer include the transurethral resection of bladder tumour (TURBT) and cystectomy. These treatments are highly invasive and are accompanied with their own set of complications, such as the risk of tumour recurrence in TURBT and the reduced quality of life in cystectomy, particularly one that involves the complete removal of the bladder. As such, there is a need for new treatments of bladder cancer that are less invasive and more reliable.

One such method with promising potential is nanoparticle-assisted photothermal therapy [2–7]; a thermal ablation technique that utilises light in the form of laser in the near-infrared (NIR) range to induce

* Corresponding author. Ascend Technologies Ltd, Southampton Science Park, 2 Venture Road, SO16 7NP, Southampton, United Kingdom.
E-mail addresses: viktor@ascendtechnologies.co.uk (V. Popov), alfano.massimo@hsr.it (M. Alfano), ooi.ean.hin@monash.edu, eanhin@ascendtechnologies.co.uk (E.H. Ooi).

https://doi.org/10.1016/j.compbiomed.2021.104881
Received 1 August 2021; Received in revised form 1 September 2021; Accepted 16 September 2021
Available online 20 September 2021

hyperthermic conditions inside the bladder. The use of NIR laser alone is typically insufficient to cause significant rise in tissue temperature due to the high photon scattering in tissues. Hence, nanoparticles are used as photoabsorbers to help convert the optical energy into heat inside the tissue. Among the various nanoparticles available, gold nanorods (GNR) have been shown to be good photoabsorbers due to their tunable properties [8–11]. By manipulating the aspect ratio of each GNR, the absorption of light can be tuned to peak in the NIR region for optimum heating inside the tissue. Furthermore, GNR can be bio-conjugated with cancer-targeting antibodies that allow them to selectively attach to the cancer cells [12–14]. This leads to a localised and targeted cancer treatment. Specifically, gold is selected over other noble metals because of their good bio-conjugation abilities, which makes them highly suitable for this treatment.

Various studies have demonstrated the ability of GNR-assisted photothermal therapy (GNR-PTT) to induce sufficient hyperthermic and ablative effects in animal models, primarily of mice [12,15,16]. In mice, the tumour can be established by injecting tumour cells in organ-specific microenvironment and the tumour develops in the organ (orthotopic). In the case of orthotopic bladder cancer, the tumour can grow in any region of the bladder, close to skin surface, where laser irradiation takes places or deeper from skin surface. While this is likely due to the difficulty in growing and monitoring tumour growth at deeper regions of the bladder, in reality, bladder cancer can grow anywhere along the bladder lining. As a result, this creates uncertainty on the suitability of GNR-PTT for treating bladder cancer that grows at deeper regions of the bladder.

To address this uncertainty, the present study sets out to investigate the efficacy of GNR-PTT for the treatment of bladder cancer in mice for cases where the tumour grows at different parts of the bladder. It is important to note that the goal of GNR-assisted photothermal therapy is to produce controlled heating of the targeted tumour to 46 °C to achieve hyperthermia. However, in the present study, thermal coagulation was selected as the limiting point, and the formation of thermal coagulation inside the tissue was modelled as the threshold not to exceed. Investigations were carried out *in-silico* since computational models give users the flexibility to place the tumour at a desired location along the bladder lining. The optical and thermal simulations were carried out using the Monte Carlo and finite element methods, respectively. Three different locations of tumour growth that are characterised by the different depths from the skin surface were considered. For each location, the efficacy of GNR-PTT was investigated by quantifying the temperature increase and the amount of thermal damage sustained by the tumour, the bladder, and the surrounding tissues.

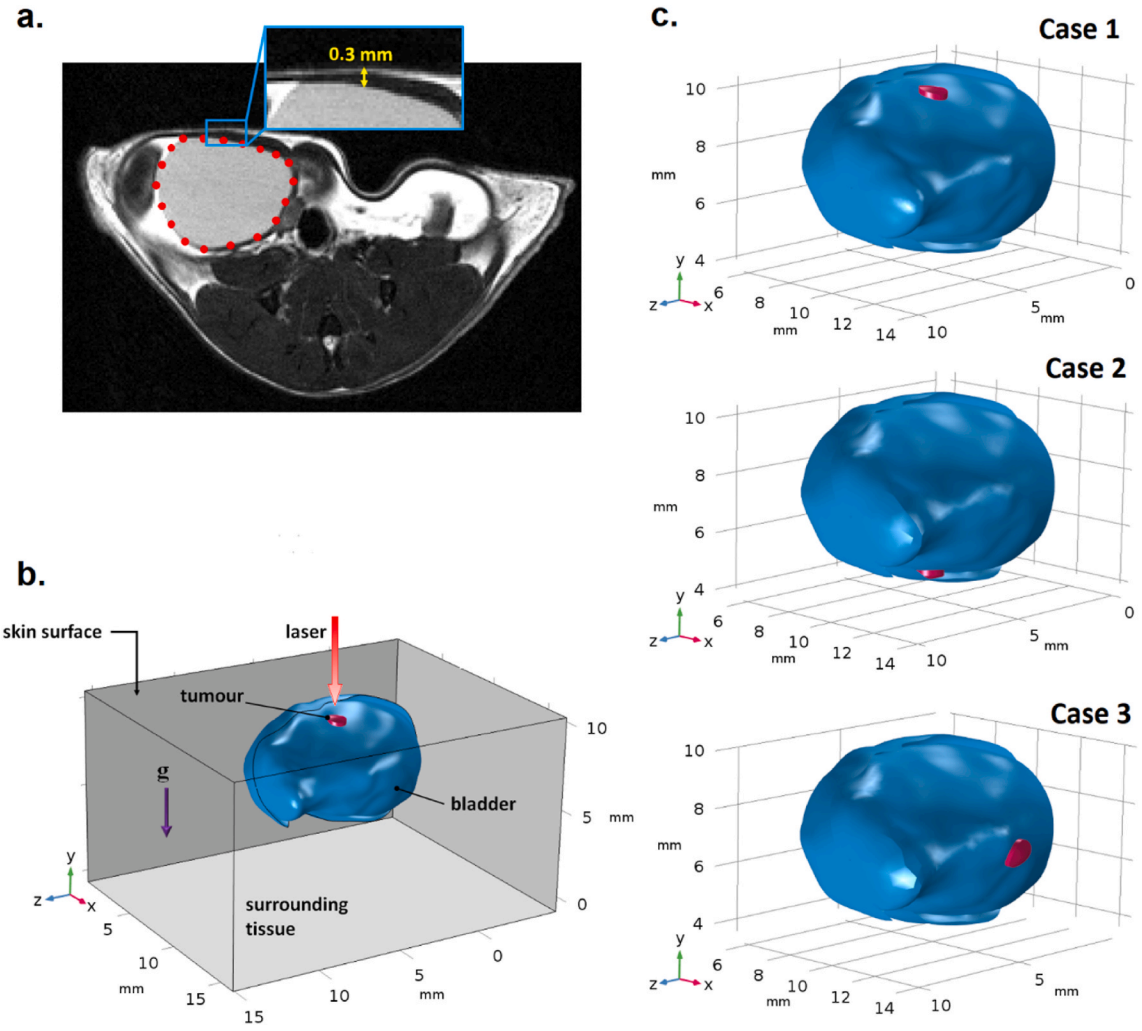

Fig. 1. a) Representative MRI image of morphological mice bladder treated with saline (T1 weighted image, Bruker Pharmascan 7T). The red dots outline the bladder of the mouse while the yellow arrow indicates the thickness between the bladder and skin surface; b) the 3D Model of the bladder and the surrounding tissue used in the present study; c) the different positions of the tumour considered in the present study. In all cases, the mouse is assumed to lie on its back such that gravity is in the negative *y*-direction.

2. Methodology

2.1. Model geometry

An anatomically accurate bladder model was constructed based on the MRI images obtained from a female C57/BL6 mouse at 8 week of age (IACUC #942). Using ImageJ, points were annotated along the outline of the bladder, such as shown in Fig. 1a. This was carried out for a total of 10 slices that contain the bladder. The positions of the points were delineated to ensure an accurate representation of the mouse bladder. Following that, the coordinates of the points were extracted and imported into SolidWorks. The *loft* feature was employed to form a 3D model of the bladder with a uniform thickness of 0.35 mm [17].

The 3D bladder geometry was then exported to COMSOL Multiphysics, where a cuboid of length, width, and height of 20, 16 and 11 mm, respectively, was constructed around the bladder to represent the anatomically homogeneous surrounding tissue. This is illustrated in Fig. 1b. The bladder was positioned within the cuboid at a depth of 0.3 mm from the surface at which laser irradiation is introduced (see Fig. 1b). This depth represents the actual depth between the surface of the bladder and the skin, as viewed from the MRI image, see Fig. 1a. Since the MRI scans were obtained from a healthy mouse, an ad hoc sub millimeter tumour with a shape that resembles a cylinder and an estimated volume of 0.192 mm^3 was generated and placed at three different locations of the bladder. The first location (Case 1) corresponds to the tumour located at the bladder wall just beneath the surface of the skin. The second location (Case 2) places the tumour at the bottom half of the bladder. At the third location (Case 3), the tumour is located at the side of the bladder. These locations are shown in Fig. 1c. The finalised model consists of four domains, i.e., the surrounding tissue, the bladder, the tumour, and the urine.

The process of attaching the GNRs to the tumour was not considered in the present study. Instead, the GNRs are assumed to be homogeneously distributed inside the tumour domain.

2.2. Monte Carlo simulations

Laser propagation inside the tissue was simulated using the Monte Carlo method, which is widely regarded as the gold standard for modelling light propagation [18–20]. Details of the Monte Carlo algorithm are already published in several textbooks and online sources; hence, they will not be presented here. In the present study, the Monte Carlo method was implemented using the open-source code ValoMC [20]; a mesh-based Monte Carlo algorithm that simulates the propagation of light in geometries that are defined by a series of unstructured mesh, such as triangles (in 2D) and tetrahedrons (in 3D). This is especially useful in the present study as the complex shape of the bladder can be easily discretised into tetrahedrons. The algorithm requires four inputs, i.e., the absorption coefficient (μ_a), the scattering coefficient (μ_s), the scattering anisotropic factor (g) and the refractive index (n). Upon solving, the algorithm outputs the fluence distribution, which can be exported into COMSOL Multiphysics for the heat transfer simulations to be carried out.

2.3. Heat transfer model

Heat transfer inside the tissue (tumour, bladder and surrounding tissue) can be expressed using the Pennes bioheat equation [21,22]:

$$\rho_t(T_t)c_t(T_t)\frac{\partial T_t}{\partial t} = \nabla\cdot(k_t(T_t)\nabla T_t) + \rho_b c_b \omega_b(\Omega)(T_b - T_t) + \mu_{a,t}\Phi_t P_{laser} \quad (1)$$

where T is temperature, $\rho_t(T)$, $c_t(T)$ and $k_t(T)$ represent the temperature-dependent density, specific heat and thermal conductivity of tissue respectively, ρ_b and c_b are the density and specific heat of blood, respectively, ω_b represents the damage-dependent blood perfusion rate, T_b is the arterial blood temperature, $\mu_{a,t}$ is the absorption coefficient, Φ_t is the fluence distribution obtained from the Monte Carlo simulations and P_{laser} is the laser power. It is noteworthy that the metabolic heat generation term that is usually present in the bioheat transfer equation has been omitted due to its negligible contribution when compared to the heat generated during photothermal ablation.

Heat transfer inside the urine domain is described using the conduction-convection equation:

$$\rho_f(T_f)c_f(T_f)\frac{\partial T_f}{\partial t} + \mathbf{u}\cdot\nabla T_f = \nabla\cdot\left(k_f(T_f)\nabla T_f\right) + \mu_{a,f}\Phi_t P_{laser}, \quad (2)$$

where the subscript 'f' represents urine inside the bladder and $\mathbf{u} = (u, v, w)$ is the vector field describing the velocity of urine flow inside the bladder in the x-, y- and z-directions. The velocity field can be obtained by solving in the urine domain the Navier-Stokes equations given by:

$$\rho_f(T_f)\frac{\partial \mathbf{u}}{\partial t} + \rho_f(T_f)(\mathbf{u}\cdot\nabla\mathbf{u}) = -\nabla p + \mu_f\nabla^2\mathbf{u} + \rho_f(T_f)\mathbf{g}, \quad (3)$$

$$\rho_f\nabla\cdot\mathbf{u} = 0, \quad (4)$$

where, p is pressure, μ_f is the dynamic viscosity of urine and $\mathbf{g}$ is the gravitational acceleration that acts in the negative y-direction. The last term on the right-hand side of Eq (3) represents the thermally induced buoyant forces acting on urine inside the bladder and can be described using the Boussinesq approximation:

$$\rho_f(T_f) = \rho_{ref}\left[1 - \beta_f(T_f - T_{ref})\right], \quad (5)$$

where ρ_{ref} is the density evaluated at reference temperature $T_{ref} = T_{body} = 37°C$ and β_f is the thermal expansion coefficient of urine. The urine was assumed to be a Newtonian fluid, while flow of urine inside the bladder was assumed to be laminar with negligible viscous dissipation.

2.4. Cell death model

As pointed out in Section 1, it is the aim of this study to achieve coagulative necrosis as the threshold that should not be breached during GNR-assisted photothermal. To describe thermal coagulation, the differential equation describing the rate of thermal coagulation formation was used [23]:

$$\frac{d\Omega(x,y,z,t)}{dt} = Ae^{-\frac{\Delta E}{R_c T(x,y,z,t)}}, \quad (6)$$

where Ω is a parameter that quantifies the amount of tissue coagulation, A is the frequency factor, ΔE is the activation energy required to cause irreversible thermal damage and R_c is the universal gas constant. The values of Ω calculated from Eq (6) represent the percentage probability of cell destruction at a specific area due to increase in temperature. A value of $\Omega = 1$ is commonly used to represent 63% of cell death [24]. In the present study, a threshold of $\Omega = 4.6$, which represents a 99% probability of cell death was used to quantify thermal damage [25].

2.5. Initial condition

Light propagation was assumed to occur at a much shorter timescale than heat transfer; hence, the Monte Carlo simulations can be decoupled from the heat transfer simulations. The initial temperature of the model was obtained by solving Eqs (1)–(5) at steady state without any exposure to laser, i.e., by prescribing the time derivative in the left-hand side of Eqs (1)–(3) to be zero and by letting $P_{laser} = 0$.

2.6. Boundary conditions

The skin surface was assumed to be exposed to ambient conditions, where heat transfer via convection takes place, hence, a Robin condition was prescribed:

$$-k_t(T_t)\frac{\partial T_t}{\partial n} = h_{amb}(T_t - T_{amb}), \tag{7}$$

where h_{amb} is the convective heat transfer coefficient between the skin and the ambient, and T_{amb} is the ambient temperature. The bottom surface of the surrounding tissue was assumed to be sufficiently far from the laser focal zone for normo-thermoregulation to successfully maintain the temperature here at basal level. Therefore, the boundary condition across this surface is given by:

$$T_t = T_{body} = 37^{\circ}\mathrm{C}, \tag{8}$$

For the hydrodynamics model, the stationary no slip condition was prescribed across the inner surfaces of the bladder wall, such that:

$$\mathbf{u} = 0. \tag{9}$$

2.7. Material properties

2.7.1. Thermal properties

The thermal properties used in the present study are listed in Table 1. Except for the tumour, the values presented in Table 1 were obtained from IT'IS database [26]. Due to the lack of information regarding bladder cancer thermal properties, the properties of liver cancer were used instead as the thermal properties of non-cancerous liver and bladder tissues differ by less than 1.5% [34]. Because of the low GNR volume fractions (v/v) considered in the present study (see Section 3.0), the presence of the GNR was assumed to have negligible influence on the thermal properties of the tumour. These volume fractions are in line with the ranged used in previous literature studies [9,27,28]. All parameters were assumed to be homogeneous, isotropic and independent of the physical variables of the present study, except for the thermal conductivity, which was assumed to increase linearly with temperature at a rate of 1.5% per increase of 1 °C [29]. This assumption was applied to all the domains including the urine inside the bladder.

Studies on porcine have shown that the blood perfusion in kidneys increases nonlinearly with temperature [30]. Below 45 °C, tissue responds to the increase in temperature by increasing the blood flow through vasodilation [31]. Further increase in temperature results in vascular stasis, which eventually leads to a decrease in blood perfusion. Blood perfusion stops when complete cell necrosis has occurred. This temperature-dependent behaviour of blood perfusion can be expressed as a piecewise homogeneous function of Ω given by Refs. [30,32]:

$$\omega_b(\Omega) = \begin{cases} 0.3\omega_{b,ref}\left(1-e^{-\Omega}\right) + 0.01\omega_{b,ref}, & \Omega \le 0.02 \\ -0.13\omega_{b,ref}\left(1-e^{-\Omega}\right) + 0.0186\omega_{b,ref}, & 0.02 < \Omega \le 0.08 \\ -0.0079\omega_{b,ref}\left(1-e^{-\Omega}\right) + 0.00884\omega_{b,ref}, & 0.08 < \Omega \le 3.5 \\ -0.0387\omega_{b,ref}\left(1-e^{-\Omega}\right) + 0.0387\omega_{b,ref}, & 3.5 < \Omega \le 4.6 \end{cases}, \tag{10}$$

where $\omega_{b,ref}$ represents the blood perfusion rate at body temperature.

Eq (10) was applied only to the bladder and surrounding tissues, but not to the tumour. This is due to the limited ability of tumour tissues to increase its blood flow in response to hyperthermia [31]. For the tumour, a more conservative form of damage-dependent blood perfusion was adopted:

$$\omega_b(\Omega) = \omega_{b,ref} \times \begin{cases} 1, & \Omega < 4.6 \\ 0, & \Omega \ge 4.6 \end{cases}, \tag{11}$$

Eq. (11) implies that blood perfusion is only present in tissues that have not been completely ablated.

Table 1
Thermal properties employed in the present study.

Parameter	Value	Source
Bladder		
Thermal conductivity, k (W/m^{2}K)	0.52	[26]
Density, ρ (kg/m^3)	1086	[26]
Specific heat, c (J/kgK)	3581	[26]
Blood perfusion rate, ω_b (1/s)	0.0014	[26]
Frequency factor, A (1/s)	3.3×10^{38}	[30]
Activation energy, ΔE (J/mol)	2.57×10^5	[30]
Tumour		
Thermal conductivity, k (W/m^{2}K)	0.49	[52]
Density, ρ (kg/m^3)	1090	[52]
Specific heat, c (J/kgK)	3421	[52]
Blood perfusion rate, ω_b (1/s)	0.00165	[52]
Frequency factor, A (1/s)	1.46×10^{52}	[53]
Activation energy, ΔE (J/mol)	3.43×10^5	[53]
Surrounding tissue		
Thermal conductivity, k (W/m^{2}K)	0.21	[26]
Density, ρ (kg/m^3)	911	[26]
Specific heat, c (J/kgK)	2348	[26]
Blood perfusion rate, ω_b (1/s)	0.0005	[26]
Frequency factor, A (1/s)	1.61×10^{45}	[54]
Activation energy, ΔE (J/mol)	3.06×10^5	[55]
Urine		
Thermal conductivity, k (W/m^{2}K)	0.56	[26]
Density, ρ (kg/m^3)	1024	[26]
Specific heat, c (J/kgK)	4178	[26]
Thermal expansion coefficient, β_f (1/K)	3.374×10^{-4}	[56]
Dynamic viscosity, μ_f (Pa.s)	0.0007	[56]
Constants		
Universal gas constant, R_c (J/molK)	8.314	
Ambient temperature, T_{amb} (°C)	25	
Ambient convection coefficient, h_{amb} (W/m^{2}K)	3	

Table 2
Optical parameters and the peak absorption and scattering coefficients at φ = 0.001, 0.005 and 0.01%.

Parameter	Value	Source
Free electron density, n_o (1/m^3)	5.9×10^{28}	[a]
Permittivity of vacuum, ε_o (F/m)	8.85×10^{-12}	[a]
Electron charge, e (C)	1.6×10^{-19}	[a]
Mass of electron, m_e (kg)	9.1×10^{-31}	[a]
Fermi velocity, v_F (m/s)	1.39×10^6	[a]
Mean free path of electron (m)	42×10^{-9}	[50]
Absorption coefficient, μ_a (1/mm)		
Bladder	0.02	[34]
Surrounding tissue	0.105	[57]
Urine	0.002	[35]
Tumour embedded with GNR		
φ = 0.001%	4.29	¥
φ = 0.005%	21.47	¥
φ = 0.01%	42.93	¥
Scattering coefficient, μ_s (1/mm)		
Bladder	4.41	[34]
Surrounding tissue	11.16	[57]
Urine	1	[35]
Tumour embedded with GNR		
φ = 0.001%	0.052	¥
φ = 0.005%	0.261	¥
φ = 0.01%	0.521	¥

¥ Estimated using Mie-Gans theory.
[a] Constants.

2.7.2. Optical properties

The optical properties used in this study are presented in Table 2. The refractive indices and scattering anisotropic factors of all tissues were chosen to be 1.4 and 0.9, respectively [33]. It should be noted that optical properties for mice bladder are not available in literature. Hence, the values used are that of a generalised bladder model developed from porcine [34]. For the urine, the absorption coefficient, scattering coefficient and refractive index were assumed to be that of water. The scattering anisotropic factor for the urine was chosen to be 1, implying that photon propagation inside the urine domain is a purely forward scattering motion [35].

Unlike thermal properties, the influence of the GNR inside the tumour on the optical properties of the domain cannot be ignored. These values were obtained from the Mie-Gans theory [36] and they vary depending on the volume fraction of GNR inside the tumour. In the present study, the size of all the GNR was assumed to be uniform, with a diameter of 10 nm and an aspect ratio of 3.8, giving peak absorbance at a wavelength of 778 nm. For more details on the calculation of the tumour-GNR optical properties, readers may refer to Appendix A.

2.8. Mesh convergence

In computational simulations, mesh convergence studies are standard but paramount practices to ensure that the results obtained are not affected by mesh size discrepancies. In addition, they help to determine the minimum number of elements that can be used to reduce computational taxation. In this study, mesh convergence was obtained by systematically decreasing the maximum element size of the different domains. The criteria for convergence were determined by comparing the values of temperature and the velocity magnitude along the lines that cross the centre of the tumour (from top to bottom) and across the centre of the bladder (from left to right) as shown in Fig. 2a. Fig. 2b presents the convergence results for the different mesh settings tested. The final mesh configuration selected was mesh 4, which resulted in approximately 4.5×10^5 elements. Though the results from mesh 3 and mesh 4 are near identical, the difference in computational time was minute, hence, the finer mesh configuration was selected.

2.9. Model validation

To validate the accuracy of the dynamic model of GNR-PTT, an experiment involving the irradiation of an aqueous solution containing scalar concentrations of GNR (ranging from 0.25 to 1 mM) was carried out. The setup of the experiment is shown in Fig. 3a. A cuvette measuring $10 \times 10 \times 45$ mm^3 was used to store 0.5 ml of aqueous GNR solution. An 808 nm continuous wave laser (Thorlabs Diode 808 CW) with a beam diameter of 1 mm was used to irradiate the solution from the side (see Fig. 3b). This wavelength was chosen as it is the most effective for the GNRs used in this study. A thermal image (Heimann Sensor model HTPA80 $\times$ 64d) was used to record the change in temperature at the cuvette's wall during laser irradiation. CTAB-coated GNRs (GNRs@CTAB) were prepared following the procedure described by Ye et al. [37], involving the growth of ultrasmall gold seeds into an aqueous solution of CTAB and sodium oleate containing gold precursor salt, silver ions and ascorbic acid as reducing agent. The GNR used had an average length of 24.9 nm and aspect ratio of 3.99. Irradiation was carried out for 15 min on GNR solutions at concentrations of 0.25, 0.5 and 1 mM, 0.5 mM and 0.25 mM, which corresponded to volume fractions of 0.000941, 0.000569 and 0.000315% v/v respectively. The laser power selected were: 0.2, 0.3 and 0.4 W, leading to a power density of 25, 38 and 51 W/cm^2 respectively.

For the validation study, a model of the cuvette was created, as shown in Fig. 3c. Simulations of the irradiation process were carried out using the framework presented in Sections 2.2 and 2.3 using parameters obtained from the experiments. Nevertheless, two parameters from the experiments could not be ascertained, namely the thermal properties of the cuvette and the convection heat transfer coefficient (h_{amb} in Eq (7)) between the walls of the cuvette and the ambient. While it is known that the cuvette was manufactured from crystal clear polystyrene, the exact values of the thermal properties are unknown. Hence, the value used in this study were obtained from literature, i.e., $k_c = 0.13$ (W/mK), $c_c = 1300$ (J/kgK) and, $\rho_c = 1050$ (kg/m^3) [38]. For the convection heat transfer coefficient, a trial-and-error approach was employed to calibrate the value of h_{amb} that best fit the temperature for a given experiment, in this case, the study with laser power of 0.2 W and GNR volume fraction of 0.000569%. This value was then used to simulate all the other experiments and the results comparing the transient temperature distribution at the cuvette wall during the 15 min irradiation are shown in Fig. 3c. Good agreement between the numerical results and the experimental measurements was obtained, which supports the accuracy of the modelling framework presented above.

3. Results

According to Ooi et al. [39], a proper combination of laser power and GNR concentration is required to provide an effective treatment outcome. An effective treatment outcome in this case is defined by the ability to destroy the tumour while preserving as much as possible the bladder and the surrounding tissues. Hence, a preliminary study was carried out to determine the right combination of GNR concentration and laser power to be used for treating the tumours at different positions inside the bladder. Results from the preliminary study (results not

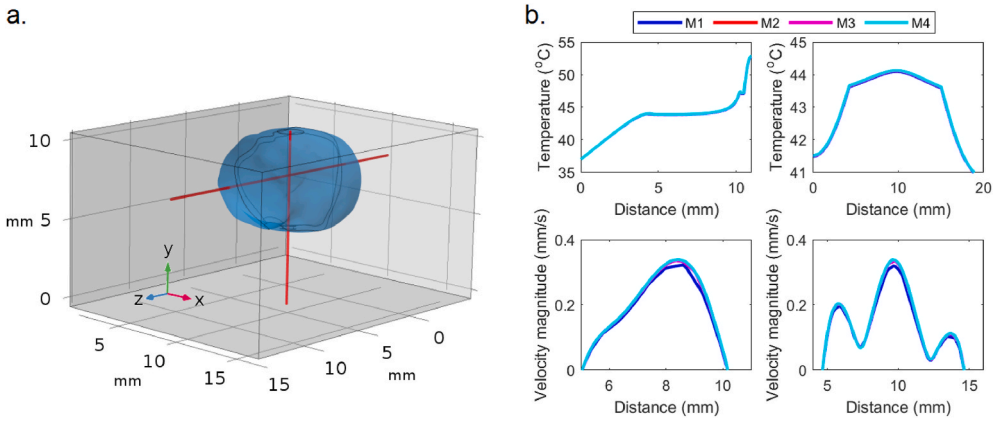

Fig. 2. a) Lines where temperature and velocity magnitude are plotted to check for mesh convergence. The vertical line passes through the centre of the tumour (for Case 1) while the horizontal line passes through the centre of the bladder. b) Mesh convergence results for temperature and velocity magnitude. The graphs on the left are the results of the vertical line and the graphs on the right are results of the horizontal line.

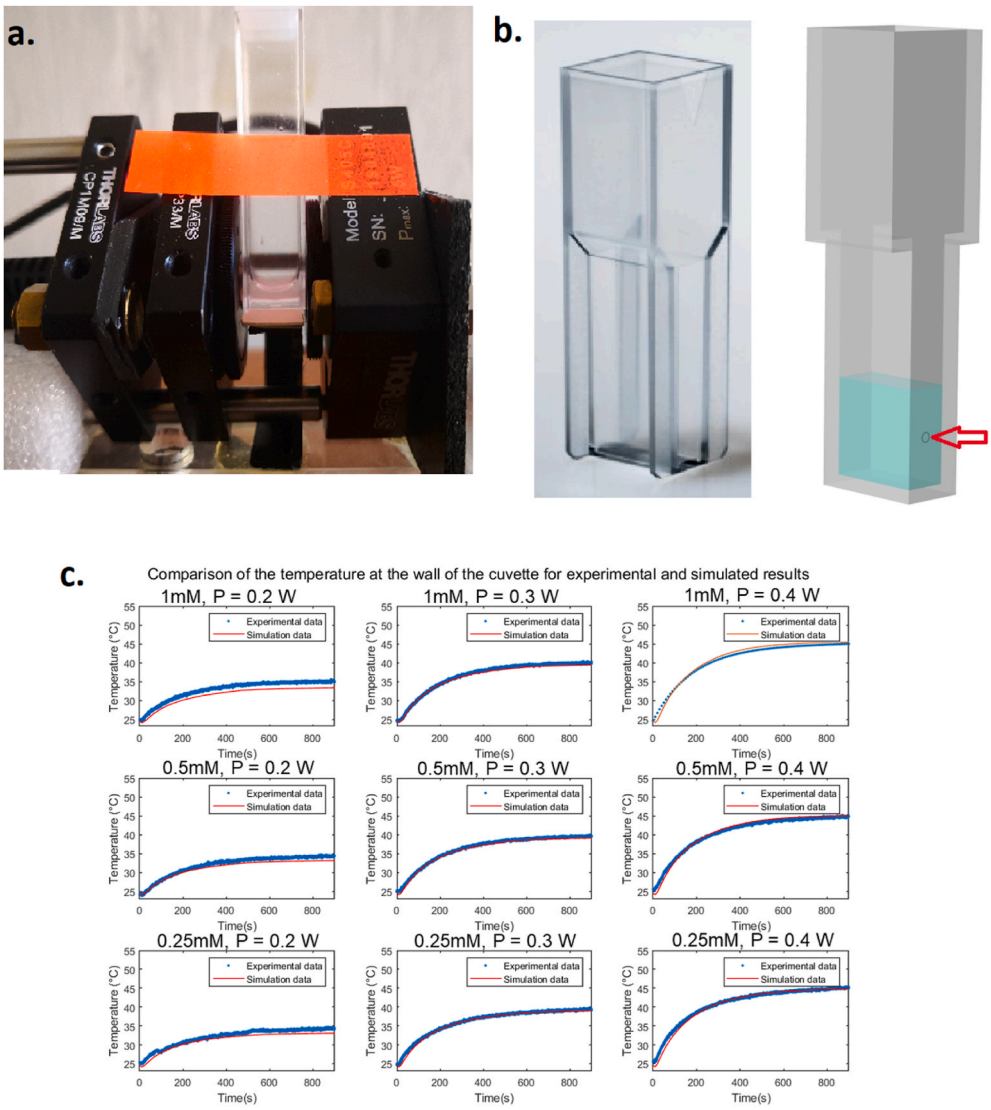

Fig. 3. a) Setup of model validation experiment. b) Actual cuvette and model geometry of the cuvette. The dark blue cuboid represents the aqueous suspension of GNR and the red arrow indicates direction of laser irradiation. c) Temperature distribution for the wall of the cuvette for experimental and simulated cases. From left to right, each column represents different laser powers. From top to bottom, each row represents different volume fractions of GNR.

shown here) showed that a GNR volume/tumour volume fraction of 0.01%, hereafter referred to as 0.01% v/v, and laser power of 0.3 W are required to attain an effective treatment outcome. This combination was subsequently used in all the simulations investigating the effects of different tumour positions.

3.1. *Effects of tumour position*

Fig. 4a illustrates the contours of the temperature distribution across the surfaces of the bladder and tumour, and the surrounding tissue for $z < 5$ mm after 30 s of laser irradiation. The temperature contours are capped at 45°C for better visualisation. In all three cases, peak temperatures occur at the surface of the skin, where laser penetrates (see red arrows). Case 1 produced the highest average tumour temperature (44.9°C) after 30 s of laser irradiation, which is not surprising since it is the closest to the laser source. There is not much difference in the average tumour temperature between Cases 2 and 3 (39.5 vs 40.2°C). The lower tumour temperature in these cases may be explained by the greater distance of these tumours from the skin surface, which results in greater photon scattering and absorption by the bladder and surrounding tissue, leaving only a small portion to be absorbed by the GNRs inside the tumour.

A region of elevated temperature beneath the bladder is evident in Cases 1 and 2, as indicated by the yellow arrows. This is postulated to be due to the convective currents of urine inside the bladder, which facilitates the transfer of heat across the bladder and urine domains. In Case 3, temperatures exceeding 45°C were observed across a large portion of the surrounding tissue near the site of laser irradiation. This was not observed in Cases 1 and 2. Furthermore, the region of elevated temperature beneath the bladder in Cases 1 and 2 (see yellow arrows) was not found in Case 3. Fig. 4b illustrates the contours of the temperature distribution after 600 s of laser irradiation. The highest average tumour temperature was found for Case 1 (62.9°C), followed by Case 2 (57.0°C) and Case 3 (56.2°C). On the other hand, the highest overall tissue temperature was found for Case 3 (80.0°C), followed by Case 1 (66.9°C) and Case 2 (63.7°C). In all three cases, the peak temperatures occurred at the site of laser irradiation.

The temperature findings above are unexpected for two reasons: 1) the tumour in Case 2 is further from the laser source than in Case 3, yet the average temperature achieved is higher, and 2) the tumour in Case 1 is nearer to the laser source than in Case 3, yet the maximum temperature at the skin surface is lower.

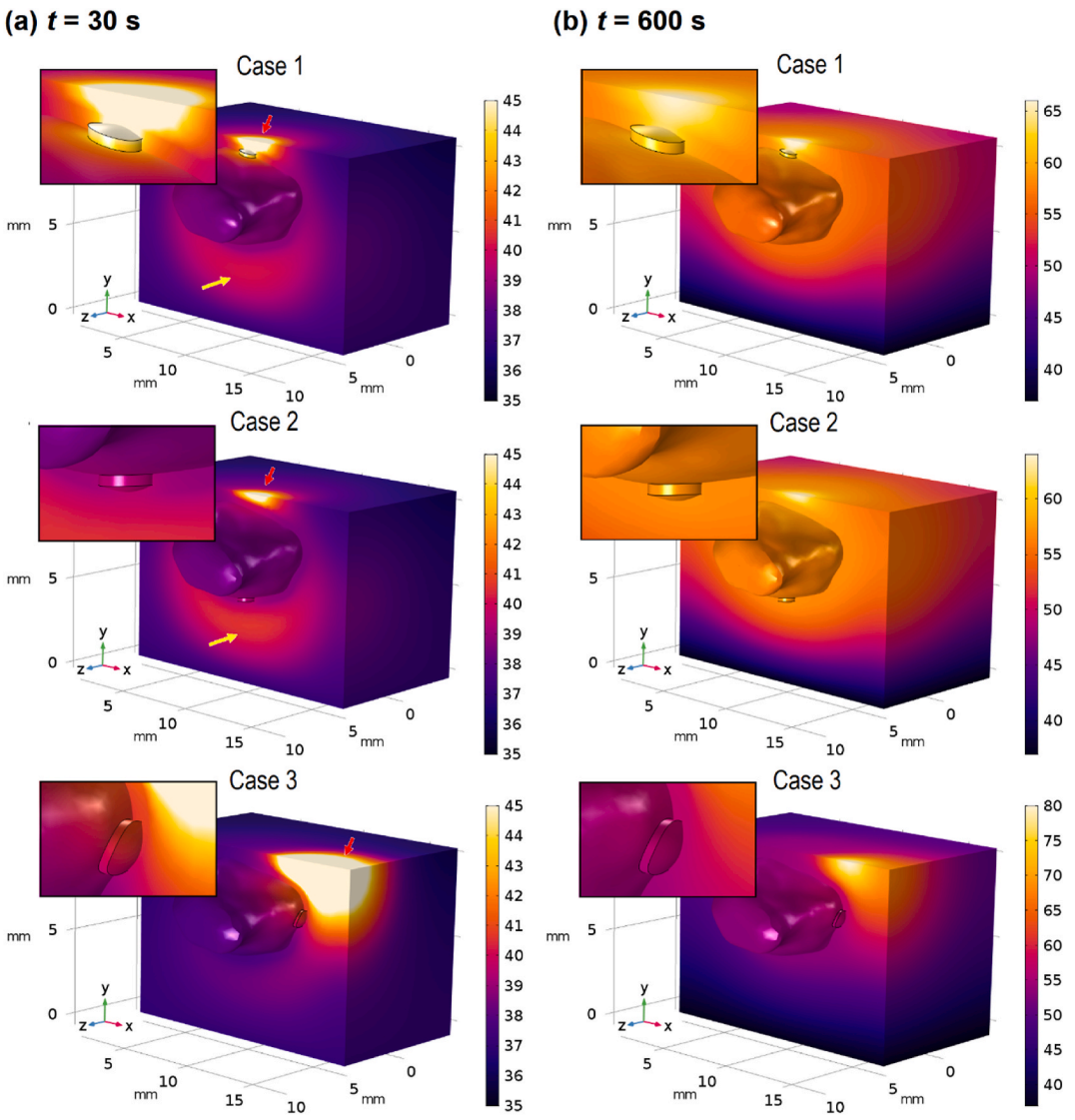

Fig. 4. Contours of the temperature distribution in °C across the tumour and bladder, and across the surrounding tissue for $z < 5$ mm at a) $t = 30$ and b) $t = 600$ s after laser irradiation for Cases 1, 2 and 3. Yellow arrows indicate the region of surrounding tissue beneath the bladder with elevated temperatures.

To explain these results, one must look at the type of tissue(s) that the laser must travel through before reaching the tumour, along with the orientation of the tumour with respect to the incident laser. In Case 2, the laser passes through a small section of the surrounding tissue and bladder, before going through the urine and eventually reaching the tumour. The low absorption and scattering coefficients of the urine (see Table 1) and the small thicknesses of the surrounding tissue and bladder meant that the photons experienced lower absorption and scattering on the way to the tumour. On the other hand, the photons in Case 3 must travel through a large section of the surrounding tissue before reaching the tumour. From Table 2, one may note that the absorption coefficient of the surrounding tissue is approximately 5 and 50 times larger than the ones for bladder and urine, respectively. Similarly, the scattering coefficient is approximately 2.5 and 11 times larger than the ones for bladder and urine, respectively. This, coupled with large thickness of the surrounding tissue that the laser irradiation must pass through, eliminates most of the photons by absorption and scattering, allowing for a small quantity to reach the tumour to be absorbed by the GNRs.

The absorption of photons by the surrounding tissue in Case 3 is evident from the temperature plot in Fig. 4. Although the laser irradiation must pass through the surrounding tissue in Case 1, the small thickness limits the amount of absorption and subsequently the heating. This explains why the peak temperature in Case 3 is higher than in Case 1. The lower absorption as the result of fewer number of photons reaching the tumour in Case 3 can be confirmed by the estimation of the total energy absorbed by the tumour over the 600 s laser irradiation. This can be obtained by performing a temporal-volumetric integral of the last term on the right-hand-side of Eq (1). For Cases 1, 2 and 3, values of the total energy absorbed were found to be 27.2, 3.61 and 3.47 J, respectively.

Fig. 5 plots the contours of thermal damage obtained following 600 s of laser irradiation. Thermal damage in this case is represented by zones in red, i.e., when $\Omega > 4.6$. Only Case 1 demonstrated complete ablation of the tumour, which is marked by the complete thermal damage achieved. A small portion of the bladder and the surrounding tissue next to the tumour were also thermally destroyed as the result of heat conduction from the tumour. Case 2 failed to record any thermal damage in both the tumour and the surrounding tissue where laser irradiation takes place. Case 3 also failed to produce any thermal damage to the tumour. However, a large portion of the surrounding tissue above the tumour where laser irradiates was thermally destroyed. The contours in Fig. 5 suggest that treatment of bladder cancer in mouse using GNR-PTT where laser is irradiated directly from the skin surface is effective only when the tumour is located at the bladder lining that is immediately beneath

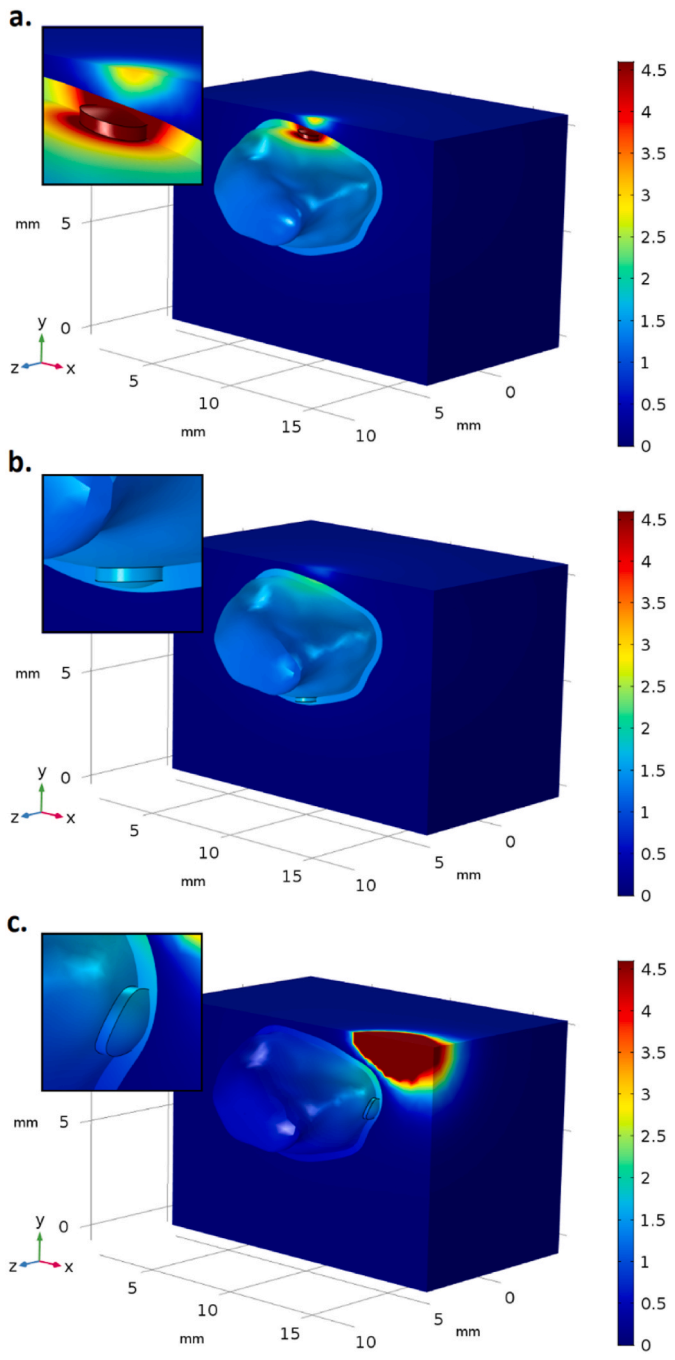

Fig. 5. Contours of the thermal damage across the tumour and bladder, and across the surrounding tissue for $z < 5$ mm at the end of treatment, $t = 600$ s, for a) Case 1, b) Case 2, and c) Case 3. The dark red region corresponding to a value of $\Omega > 4.6$ signifies the region of cell death.

the surface of the skin, i.e., Case 1.

3.2. Possibility of treating Case 2

The results presented in Section 3.1 demonstrated that it is possible to heat the tumour even when it is located at the other end of the bladder. While the heating was insufficient and complete tumour destruction was not achieved, it poses the question on whether it would be possible to raise the heating inside the tumour while maintaining a non-destructive temperature in the bladder and the surrounding tissue. In Section 3.1, the failure to generate sufficient heating may be attributed to insufficient light reaching the tumour. In theory, increasing the laser power would induce more heating in the tumour as more light can reach the tumour. At the same time, a higher laser power would also induce more heating at the site of laser irradiation. Hence, if the surface of the skin can be sufficiently cooled to prevent the formation of thermal damage, then it may be possible to increase the laser power to elevate the heating inside the tumour to levels that are sufficient to induce thermal damage.

A method to maximise the heating inside the tumour while minimising thermal damage to other parts of the tissue is proposed and assessed in this section. The method borrows the application of water-cooled system commonly used in radiofrequency ablation to combat the increase in heat generation across the probe surface. A trial-and-error approach was used to determine the combination of laser power and cooling parameters that will lead to complete tumour ablation, while eliminating any thermal damage to non-cancerous tissues. Cooling parameters are defined by the convection heat transfer coefficient (h_{amb}) and the ambient temperature (T_{amb}). Results from the trial-and-error study revealed that the combination of $P_{laser} = 1$ W, $h_{amb} = 120$ W/(m^{2}K) and $T_{amb} = 2°$C satisfies the requirement above.

Fig. 6a and b illustrate the temperature distribution obtained 30 and 600 s after laser irradiation, respectively. The high laser power resulted in larger energy absorption inside the tumour and subsequently greater heating. However, the increase in cooling along the skin surface helped to prevent excessive temperature rise at the skin surface and the surrounding tissue. Contours of the thermal damage obtained are presented in Fig. 6c, where complete ablation of the tumour domain can be observed. Some degree of thermal damage can be observed at the region of tissue next to the site of laser irradiation, but these are insufficient to induce complete thermal damage. These findings suggest that by elevating the laser power and by introducing cooling on the skin surface, a viable approach may be obtained for treating bladder cancers at deeper regions of the bladder.

3.3. Possibility of treating Case 3

A similar trial and error approach was carried out to determine if it is possible to increase the laser power and cooling on the skin surface to obtain thermal damage to the tumour while minimising damage to the surrounding tissue, similar to that seen in Case 2. Following several trials of different combination of P_{laser} (1–2 W) and h_{amb} (120–240 W/m^{2}K), it was concluded that it is not possible to treat bladder cancer in Case 3 simply by increasing P_{laser} and h_{amb}, as significant amount of thermal damage to the bladder and the surrounding tissue could not be avoided. This is shown in Fig. 7.

4. Discussion

The present study has demonstrated that the position of tumour along the bladder lining can significantly affect the treatment condition and thermal effect during GNR-PTT. Three different tumour positions were investigated. Case 1 investigates a tumour at the inner bladder wall that is immediately beneath the surface of the skin where laser irradiation takes place. Case 2 positions the tumour at the largest depth from the skin surface, while Case 3 places the tumour at the side of the bladder. The results presented in Section 3.1 showed that the tumour's location can significantly alter the outcome of the GNR-PTT.

The results obtained from the present study suggest that the type of tissue that the laser must pass through before reaching the tumour have a more significant impact on the treatment outcome than the distance of the tumour from the skin surface. In general, if the tissue that the laser passes through has high scattering coefficient, then the number of photons that reach the tumour are reduced due to the photon scattering. A high absorption coefficient can not only reduce the photons that reach the tumour, but also causes heating of the tissue, as demonstrated in Case 3. In contrast, if the tissue through which laser propagates has low absorption and scattering coefficients, then there is a smaller chance for

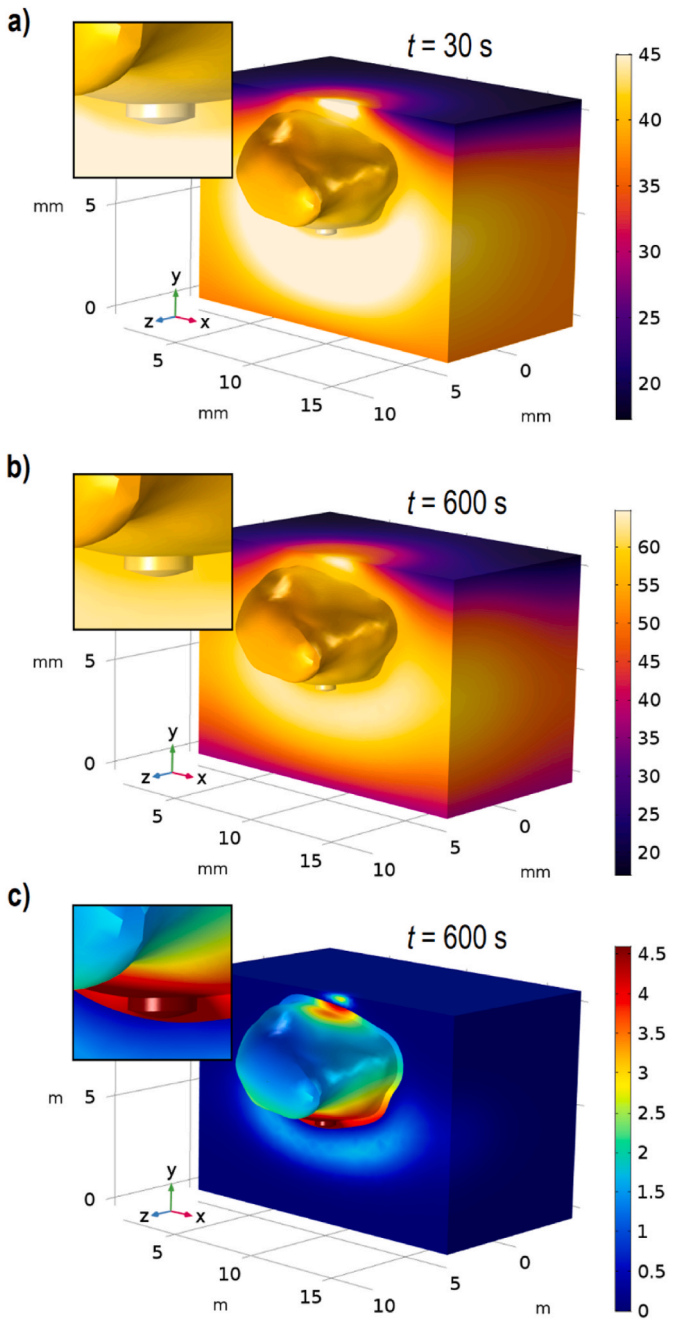

Fig. 6. Contours of the temperature distribution in °C at a) $t = 30$ s, b) $t = 600$ s and c) contours of thermal damage across the tumour and bladder, and across the surrounding tissue for $z < 5$ mm for the optimised Case 2.

the photons to be absorbed and scattered before reaching the tumour, as seen in Case 2.

For the three cases considered in the present study, if the laser power is set to 0.3 W and GNR volume fraction is 0.01% v/v, then the treatment of bladder cancer in mice using GNR-PTT is viable only for Case 1. Attempts were made to seek alternatives for treating the tumour in Cases 2 and 3. In Case 2, this was possible by increasing the laser power and by increasing cooling on the skin surface by increasing h_{amb} to 120 W/(m^{2}K). Achieving a value of $h_{amb} = 120$ W/(m^{2}K) is not unrealistic. Assuming water as the coolant, the skin surface to be flat and flow of water to be laminar, the equation relating the Nusselt (Nu), Prandtl (Pr) and Reynolds (Re) can be written as:

$$\mathrm{Nu} = 0.332\mathrm{Re}^{1/2}\mathrm{Pr}^{1/3} \tag{12}$$

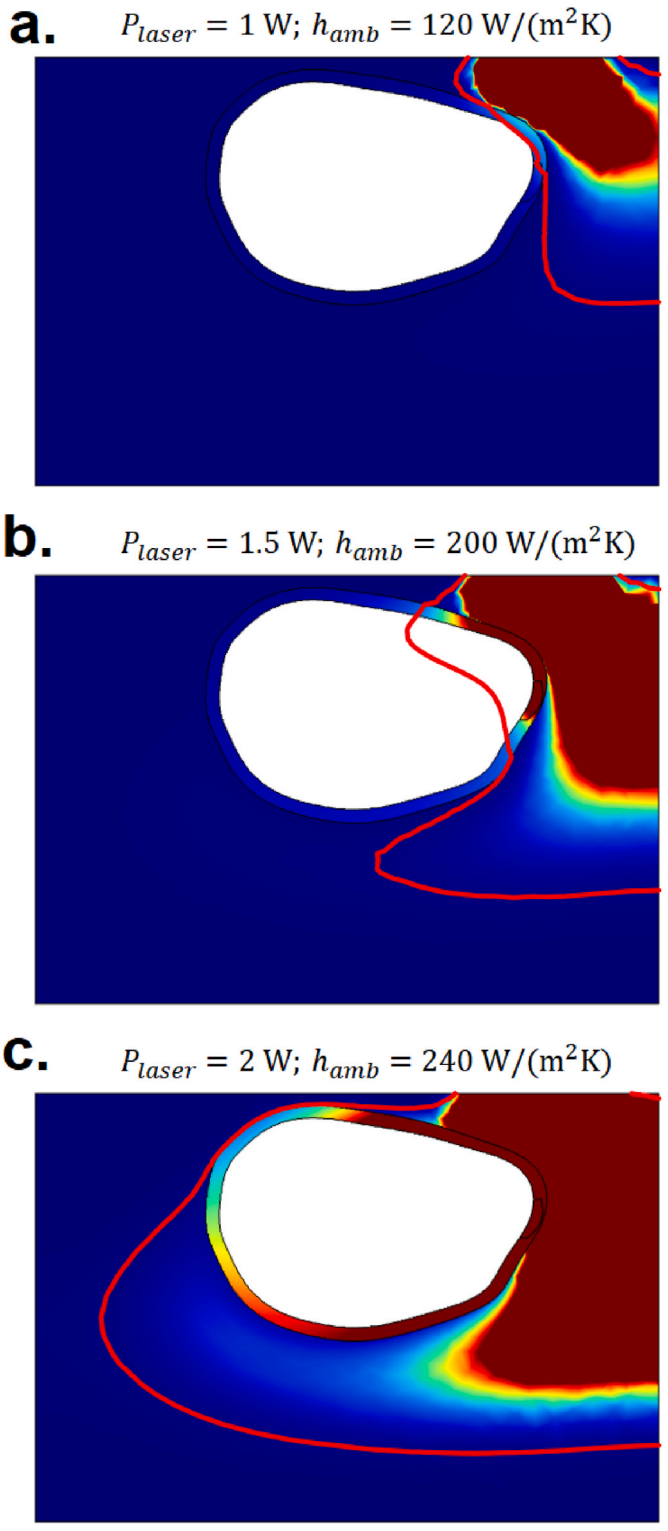

Fig. 7. Contours of thermal damage (dark red) obtained from different combinations of P_{laser} and h_{amb} in Case 3. Results show that any attempt at inducing thermal damage to the tumour is always accompanied by damages to the bladder and the surrounding tissue. The thick red line represents the 55 °C isotherm.

Using the definitions of Nu, Pr and Re of:

$$\mathrm{Nu} = \frac{h_{amb}L}{k},\ \mathrm{Pr} = \frac{\nu}{\alpha},\ \mathrm{Re} = \frac{UL}{\nu},$$

where U is the velocity of the coolant, $L = 2$ cm is the characteristic

length and $k = 0.6$ W/(mK), $\nu = 1 \times 10^{-6}$ m^2/s and $\alpha = 1.44 \times 10^{-7}$ m^2/s are the thermal conductivity, kinematic viscosity and thermal diffusivity of water, respectively. The value of U can be estimated to be approximately 2 mm/s, which is achievable. Similar cooling methods are currently being employed in cardiac ablation with water-cooled irrigation technology. Considering that this technology passes water over the heart for cardiac ablation, it should be fairly simple to employ this method for use on the skin [40].

It was however not possible to successfully destroy bladder cancer in Case 3 using the same approach without inducing severe thermal damage to the bladder and the surrounding tissue. This is because any elevation in laser power will significantly elevate the temperature of the surrounding tissue due to its higher absorption coefficient, and any attempt to reduce the elevation in temperature by increasing h_{amb} will either fail to prevent damage to the surrounding tissue or cause insufficient heating to the tumour due to intense cooling at the skin surface. Hence, alternative techniques should be explored in future studies for treating bladder cancers in mice that are similar to those in Case 3. To this extent, it might be worthwhile to consider different strategies such as the periodic heating method or the minimal invasion method [41–43]. It might be possible to reduce the heat generation in the surrounding tissue near the skin surface by providing ample time for the tissues to cool down. Alternatively, depending on the location of the tumour, one might consider heating from the inside of the urethra to minimise the volume of surrounding tissues between the laser and the tumour.

At present, no modus operandi has been defined for treatment of human bladder cancer using GNR-PTT. As such, the result in this study may provide an insight into the potential treatments of the human urinary bladder. Cases 2 and 3 suggest that external irradiation, where the laser passes through the skin to the bladder is likely unfeasible in humans. As the layer of skin and fat between the stomach and the bladder is much thicker than that of our current model, most of the photons would have been absorbed and scattered before reaching the bladder (see Supplementary Material). However, it may be possible to conduct GNR-PTT if laparoscopic surgery was made to bypass the skin and fat such that the laser is placed directly on the outer wall of the bladder. As the human bladder possesses a low absorption coefficient and a high scattering coefficient [33,34,44], the laser could potentially reach the tumour with minimal energy loss. It should be noted that further research would be require as the human bladder wall is also thicker than that of the current model.

Although the present study has successfully investigated the effects of tumour position on the treatment of bladder cancer using GNR-PTT, there are a few limitations in the present model that should be addressed in the future. Firstly, the model validation in the present study was carried out against heating experiments performed on GNR suspension in a cuvette. Although the results demonstrated good agreement, model validation against experimental studies performed on actual mice will help to raise the confidence on the accuracy and reliability of the results. Secondly, the present model assumes GNRs to be homogenously distributed throughout the tumour. While this has been the common practice when modelling GNR-PTT [39,45], how the GNRs are distributed inside or surrounding the tumour depends on the method used to introduce them into the tumour. It would be insightful in future research to consider the different variations of accumulation and excretion of nanoparticles that may be more realistic. Moreover, the present work focused on the use of GNRs for NPTT. Future studies can explore the use of different types of nanoparticles including inorganic nanoparticles [46]. Thirdly, the geometry of the tumour employed in this study was assumed to be that of a cylinder. As such, the surface area of tumour directly exposed to the laser allows for larger absorption of photons by the GNRs. However, realistic tumours are highly irregular in shape and may have reduced surface area for GNR photon absorption. Fourthly, the optical properties assigned for the mice bladder are that of a porcine bladder instead of murine. This was a necessary step taken in the present study due to the lack of available data for mouse bladder. Future studies in the form of a sensitivity analysis can help to elucidate the significance of the optical and thermal properties in the optical-thermal model developed in this paper. Lastly, the absorption and the scattering processes assumed in the present study were rather simplified. Nevertheless, the assumptions do not take away the primary finding of the present study on the feasibility of NPTT for treating cancer growing at different positions inside the mouse bladder. Future studies can explore more complex laser-tissue interaction models that can lead to a more accurate representation of the problem considered.

5. Conclusions

In this study, the effects of different tumour positions on the outcome of GNR-PTT of mice bladder tumour have been presented. The results demonstrate that the tumour position can significantly affect treatment efficacy. For a laser power of 0.3 W and a GNR volume fraction of 0.01% v/v, only the tumour in Case 1, which was located immediately below the skin surface, was successfully ablated. However, the same was not observed in Cases 2 and 3. This can be attributed to both the depth and the type of tissue that the laser irradiation must travel through. The present study proposes a potential solution to make Case 2 viable by increasing the laser power with enhanced cooling across the skin surface where laser irradiation is applied. This method is unable to work for Case 3 as the damage to the surrounding tissue could not be avoided.

Declaration of competing interest

None declared.

Acknowledgement

We wish to thank Dr. Tamara Canu (Experimental Imaging Centre, San Raffaele Scientific Institute) for the acquisition of murine MRI. This study has received funding from the European Union's Horizon 2020 research and innovation program under grant agreement No 801126 (EDIT).

Appendix B. Supplementary data

Supplementary data to this article can be found online at https://doi.org/10.1016/j.compbiomed.2021.104881.

APPENDIX A

The absorption and scattering coefficients of tumour with GNR were calculated using the Mie-Gans theory [36], which solves the Maxwell equations based on an electrostatic assumption. This assumption is valid for $D \leq \lambda/10$, where D is the diameter of the GNR and λ is the wavelength of the laser irradiation. Accordingly, the absorption and scattering coefficients of a medium embedded with GNR can be calculated using [47,48]:

$$\mu_a = \frac{2\pi\varphi}{\lambda V_{np}} \text{imag}\left(\frac{\alpha_1}{3} + \frac{\alpha_2}{3} + \frac{\alpha_3}{3}\right), \tag{13}$$

$$\mu_s = \frac{16\pi^3\varphi}{18\lambda^4 V_{np}}\left(|\alpha_1|^2 + |\alpha_2|^2 + |\alpha_3|^2\right), \tag{14}$$

where imag() represents the imaginary component, φ is the volume fraction of GNR, V_{np} is the volume of a single nanoparticle calculated by assuming the GNR to be a cylinder capped by hemispheres at both ends and α_i (for $i = 1, 2, 3$) is the polarization given by Refs. [47,48]:

$$\alpha_i = V_{np}\left[\frac{\varepsilon(\omega, D) - \varepsilon_m}{P_i(\varepsilon(\omega, D) - \varepsilon_m) + \varepsilon_m}\right], \tag{15}$$

where ε is the size- and frequency-dependent dielectric function of the GNR, ε_m is the dielectric constant of the surrounding medium and P_i is the geometrical factor. In the present study, the Kreibig-Vollmer model for calculating the size- and frequency-dependent dielectric function of GNR was adopted, which is given by Refs. [47,48]:

$$\varepsilon(\omega, D) = \varepsilon_{bulk} + \omega_p^2\left(\frac{1}{\omega^2 + \Gamma_o^2} - \frac{1}{\omega^2 + \Gamma_d^2}\right) + i\frac{\omega_p^2}{\omega}\left(\frac{\Gamma_d}{\omega^2 + \Gamma_o^2} - \frac{\Gamma_o}{\omega^2 + \Gamma_d^2}\right), \tag{16}$$

where ε_{bulk} is the frequency-dependent dielectric constant of bulk gold, and ω_p and Γ_d are given by:

$$\omega_p = \left(\frac{n_o e^2}{\varepsilon_o m_e}\right)^{\frac{1}{2}}, \tag{17}$$

$$\Gamma_d = \Gamma_o + \frac{A_s v_F}{r_{eff}}, \tag{18}$$

$$r_{eff} = \frac{4V_{np}}{S_{np}}, \tag{19}$$

where n_o is the electron density number, ε_o is permittivity of vacuum, e and m_e are the charge and mass of the electrons, respectively, v_F is Fermi velocity, A_s is the surface scattering parameter with an empirical value of 0.3, r_{eff} is effective radius, S_{np} is the surface area of a single nanoparticle and Γ_o is the free damping coefficient defined as the ratio of Fermi velocity and the mean free path of electrons [49]. The dielectric constant of bulk gold was obtained from data published by Johnson and Christy [50].

It should be noted that the Mie-Gans theory for calculating μ_a and μ_s is only valid for spheroidal nanoparticles where the geometrical factor used in Eq. (15) can be obtained using:

$$P_1 = \frac{1 - e^2}{e^2}\left[\frac{1}{2e}\ln\left(\frac{1 + e}{1 - e}\right) - 1\right], \tag{20}$$

$$P_2 = P_3 = \frac{1}{2}(1 - P_1), \tag{21}$$

where $e = [1 - (D/L)^2]^{0.5}$, P_1 is oriented in the longitudinal axis of the spheroid, while P_2 and P_3 are in the transverse directions, with $P_2 = P_3$ due to symmetry. However, the nanoparticles used in this study are GNRs shaped as spherically capped cylinders. Hence, difference in geometry must be accounted for by adjusting the geometric factor used in Eq. (15). To that extent, Prescott and Mulvaney [51] derived alternate values for P_i for GNRs which is given by:

$$\frac{1 - P_1}{P_1} = a(AR)^2 + b(AR) + c, \tag{22}$$

where AR is the aspect ratio of the nanoparticle and a, b and c are the coefficients of the quadratic function. For the GNR morphology used in this study, the coefficients of the quadratic function are $a = 0.3504$, $b = 2.0809$ and $c = -0.3035$ [51]. It is important to point out here that Eq. (22) is purely empirical, and no physical meaning should be inferred from it.

References

[1] B. Kiss, et al., Open radical cystectomy: still the gold standard for muscle invasive bladder cancer, World J. Urol. 34 (1) (2016) 33–39.

[2] M. Singh, et al., Application of gold nanorods for photothermal therapy in ex vivo human oesophagogastric adenocarcinoma, J. Biomed. Nanotechnol. 12 (3) (2016) 481–490.

[3] Z. Yang, et al., Advances in nanomaterials for use in photothermal and photodynamic therapeutics (Review), Mol. Med. Rep. 20 (1) (2019) 5–15.

[4] F. Zhou, et al., Cancer photothermal therapy in the near-infrared region by using single-walled carbon nanotubes, J. Biomed. Opt. 14 (2) (2009), 021009.

[5] A.J. Trinidad, et al., Combined concurrent photodynamic and gold nanoshell loaded macrophage-mediated photothermal therapies: an in vitro study on squamous cell head and neck carcinoma, Laser Surg. Med. 46 (4) (2014) 310–318.

[6] P. Liu, et al., Concurrent photothermal therapy and photodynamic therapy for cutaneous squamous cell carcinoma by gold nanoclusters under a single NIR laser irradiation, J. Mater. Chem. B. 7 (44) (2019) 6924–6933.

[7] H.S. Kim, D.Y. Lee, Near-infrared-responsive cancer photothermal and photodynamic therapy using gold nanoparticles, Polym. J. 10 (9) (2018) 961.

[8] Y. Wang, et al., Comparison study of gold nanohexapods, nanorods, and nanocages for photothermal cancer treatment, ACS Nano 7 (3) (2013) 2068–2077.

[9] X. Gu, et al., The effect of gold nanorods clustering on near-infrared radiation absorption, Appl. Sci. 8 (7) (2018) 1132.

[10] M.A. Mackey, et al., The most effective gold nanorod size for plasmonic photothermal therapy: theory and in vitro experiments, J. Phys. Chem. B 118 (5) (2014) 1319–1326.

[11] A.C.V. Doughty, et al., Nanomaterial applications in photothermal therapy for cancer, Materials 12 (5) (2019) 779.

[12] X. Yang, et al., The antineoplastic activity of photothermal ablative therapy with targeted gold nanorods in an orthotopic urinary bladder cancer model, Bladder Cancer 3 (3) (2017) 201–210.
[13] C.H. Chen, et al., Gold nanotheranostics: photothermal therapy and imaging of mucin 7 conjugated antibody nanoparticles for urothelial cancer, BioMed Res. Int. 2015 (2015) 813632.
[14] S.K. Cho, et al., Functionalized gold nanorods for thermal ablation treatment of bladder cancer, J. Biomed. Nanotechnol. 10 (7) (2014) 1267–1276.
[15] K. Tao, et al., Targeted multifunctional nanomaterials with MRI, chemotherapy and photothermal therapy for the diagnosis and treatment of bladder cancer, Biomater. Sci. 8 (1) (2020) 342–352.
[16] Y. Akiyama, et al., The effects of PEG grafting level and injection dose on gold nanorod biodistribution in the tumor-bearing mice, J. Contr. Release 139 (1) (2009) 81–84.
[17] L.O.S. Leiria, et al., Functional, morphological and molecular characterization of bladder dysfunction in streptozotocin-induced diabetic mice: evidence of a role for L-type voltage-operated Ca2+ channels, Br. J. Pharmacol. 163 (6) (2011) 1276–1288.
[18] V. Periyasamy, M. Pramanik, Advances in Monte Carlo simulation for light propagation in tissue, IEEE Rev. Biomed. Eng. 10 (2017) 122–135.
[19] S. Song, et al., Monte-carlo simulation of light propagation considering characteristic of near-infrared LED and evaluation on tissue phantom, Procedia CIRP 5 (2013) 25–30.
[20] A.A. Leino, et al., ValoMC: a Monte Carlo software and MATLAB toolbox for simulating light transport in biological tissue, OSA Continuum 2 (3) (2019) 957–972.
[21] H.H. Pennes, Analysis of tissue and arterial blood temperatures in the resting human forearm, J. Appl. Physiol. 1 (2) (1948) 93–122.
[22] E. H. Wissler Pennes', Paper revisited, J. Appl. Physiol. 85 (1) (1948) 35–41, 1998.
[23] F.C. Henriques Jr., Studies of thermal injury; the predictability and the significance of thermally induced rate processes leading to irreversible epidermal injury, Am. J. Pathol. 43 (5) (1947) 489–502.
[24] I.A. Chang, Considerations for thermal injury analysis for RF ablation devices, Open Biomed. Eng. J. 4 (2010) 3–12.
[25] M. Trujillo, et al., Computer modelling of an impedance-controlled pulsing protocol for RF tumour ablation with a cooled electrode, Int. J. Hyperther. 32 (8) (2016) 931–939.
[26] P. Hasgall, et al., ITIS Database for thermal and electromagnetic parameters of biological tissues, Available from: itis.swiss/database.
[27] S. Soni, et al., Role of optical coefficients and healthy tissue-sparing characteristics in gold nanorod-assisted thermal therapy, Int. J. Hyperther. 29 (1) (2013) 87–97.
[28] G. von Maltzahn, et al., Computationally guided photothermal tumor therapy using long-circulating gold nanorod antennas, Canc. Res. 69 (9) (2009) 3892–3900.
[29] M. Trujillo, E. Berjano, Review of the mathematical functions used to model the temperature dependence of electrical and thermal conductivities of biological tissue in radiofrequency ablation, Int. J. Hyperther. 29 (6) (2013) 590–597.
[30] X. He, et al., Investigation of the thermal and tissue injury behaviour in microwave thermal therapy using a porcine kidney model, Int. J. Hyperther. 20 (6) (2004) 567–593.
[31] C. Rossmanna, D. Haemmerich, Review of temperature dependence of thermal properties, dielectric properties, and perfusion of biological tissues at hyperthermic and ablation temperatures, Crit. Rev. Biomed. Eng. 42 (6) (2014) 467–492.
[32] D.J. Schutt, D. Haemmerich, Effects of variation in perfusion rates and of perfusion models in computational models of radio frequency tumor ablation, J. Med. Phys. 35 (8) (2008) 3462–3470.
[33] J.L. Sandell, T.C. Zhu, A review of in-vivo optical properties of human tissues and its impact on PDT, J. Biophot. 4 (11–12) (2011) 773–787.
[34] I. Rafailov, et al., Computational model of bladder tissue based on its measured optical properties, J. Biomed. Opt. 21 (2) (2016), 025006.
[35] L. Wang, et al., MCML—Monte Carlo modeling of light transport in multi-layered tissues, Comput. Methods Progr. Biomed. 47 (2) (1995) 131–146.
[36] R. Gans, Über die Form ultramikroskopischer Silberteilchen, Ann. Phys. 352 (10) (1915) 270–284.
[37] X. Ye, et al., Using binary surfactant mixtures to simultaneously improve the dimensional tunability and monodispersity in the seeded growth of gold nanorods, Nano Lett. 13 (2) (2013) 765–771.
[38] F. Rouabah, et al., Thermophysical and mechanical properties of polystyrene: influence of free quenching, ISRN Polymer Sci 2012 (2012).
[39] E.H. Ooi, et al., Influence of natural convection on gold nanorods-assisted photothermal treatment of bladder cancer in mice, Int. J. Hyperther. 37 (1) (2020) 634–650.
[40] D.T. Nguyen, et al., Radiofrequency ablation using an open irrigated electrode cooled with half-normal saline, JACC Clin Electrophysiol 3 (10) (2017) 1103–1110.
[41] L.A. Dombrovsky, et al., A combined transient thermal model for laser hyperthermia of tumors with embedded gold nanoshells, Int. J. Heat Mass Tran. 54 (25) (2011) 5459–5469.
[42] Y. Ren, et al., Thermal dosage investigation for optimal temperature distribution in gold nanoparticle enhanced photothermal therapy, Int. J. Heat Mass Tran. 106 (2017) 212–221.
[43] N. Manuchehrabadi, L. Zhu, Development of a computational simulation tool to design a protocol for treating prostate tumours using transurethral laser photothermal therapy, Int. J. Hyperther. 30 (6) (2014) 349–361.
[44] R. Splinter, et al., In vitro optical properties of human and canine brain and urinary bladder tissues at 633 nm, Laser Surg. Med. 9 (1) (1989) 37–41.
[45] S. Soni, et al., Investigation on nanoparticle distribution for thermal ablation of a tumour subjected to nanoparticle assisted thermal therapy, J. Therm. Biol. 43 (2014) 70–80.
[46] M.A. Khan, et al., Revisiting inorganic nanoparticles as promising therapeutic agents: a paradigm shift in oncological theranostics, Eur. J. Pharmaceut. Sci. 164 (2021) 105892.
[47] U. Kreibig, M. Vollmer, Optical Properties of Metal Clusters, Spinger-Verlag, Berlin, Germany, 1995, p. 878, 878.
[48] C. Bohren, D. Huffman, Absorption and Scattering by an Arbitrary Particle, Wiley-VCH, 2004, pp. 57–81.
[49] S.V. Gaponenko, Introduction to Nanophotonics, Cambridge University Press, Cambridge, 2010.
[50] P.B. Johnson, R.W. Christy, Optical constants of the noble metals, Phys. Rev. B 6 (12) (1972) 4370–4379.
[51] S.W. Prescott, P. Mulvaney, Gold nanorod extinction spectra, J. Appl. Phys. 99 (12) (2006) 123504.
[52] N.M. Dimitriou, et al., Prediction of gold nanoparticle and microwave-induced hyperthermia effects on tumor control via a simulation approach, Nanomaterials 9 (2) (2019).
[53] X. He, et al., Thermal therapy in urologic systems: a comparison of arrhenius and thermal isoeffective dose models in predicting hyperthermic injury, J. Biomech. Eng. 131 (7) (2009), 074507.
[54] J. Pearce, Mathematical models of laser-induced tissue thermal damage, Int. J. Hyperther. 27 (8) (2011) 741–750.
[55] N. Wright, On a relationship between the arrhenius parameters from thermal damage studies, J. Biomech. Eng. 125 (2003) 300–304.
[56] E.H. Ooi, E.Y. Ng, Simulation of aqueous humor hydrodynamics in human eye heat transfer, Comput. Biol. Med. 38 (2) (2008) 252–262.
[57] A.N. Bashkatov, et al., Optical properties of human skin, subcutaneous and mucous tissues in the wavelength range from 400 to 2000 nm, J. Phys. D Appl. Phys. 38 (15) (2005) 2543–2555.